Improved convergence characteristics of two-equation turbulence models on unstructured grids

Yair Mor-Yossef

Israeli CFD Center, Caesarea Industrial Park, 3088900, Israel

ARTICLE INFO

ABSTRACT

Second order upwind scheme discretization of Reynolds-averaged Navier–Stokes turbulence models may lack robustness, especially when using unstructured grids. Among several factors that can be traced as the reasons, preserving a monotonic solution plays a key role. A possible remedy is to smooth the variation of the turbulence model dependent variables. To that end, a square root transformation is applied to the dependent variables of a k-ω turbulence model. The new additional source diffusion terms that emerge as a result of the transformation are fully retained. Therefore, the transformed model reproduces the baseline k-ω model performance. Moreover, the transformed model greatly enhances the robustness and reliability of turbulent flow simulations on unstructured grids.

1. Introduction

Despite their relatively simple mathematical representation, Reynolds-Averaged Navier–Stokes (RANS) two-equation turbulence models present serious numerical difficulties, including convergence and positivity preservation. The common argument is that the convergence difficulties arise mainly due to the highly non-linear source term, having time scales that greatly differ from those of the convective and diffusive terms. Furthermore, in the process of convergence, non physical solutions may appear, namely, negative values of the turbulence quantities, even if the analytical solution exists and is analytically guaranteed to remain positive. The non physical solutions dramatically deteriorate the convergence rates of the overall flow solver, requiring several thousands of iterations to reach a desired convergence criterion.

According to the numerical analysis that was conducted by Jongen and Marx [1], the turbulence model convective flux may cause serious numerical difficulties. Specifically, it is the convective flux that may generate spurious oscillations, which in turn, may result in a non physical solution. The convective flux is a linear operator with regard to the turbulence model working variables. However, for high-order schemes, certain nonlinearity is introduced into the discrete approximation in an attempt to control spurious oscillations in the solution (e.g., a limiter in the widely used MUSCL schemes, or nonlinear weights in WENO schemes). These nonlinear terms may vary significantly between neighboring cells due to the local nature of the turbulence model's source term. This may especially be dramatic in the transition phase of the simulation through convergence where large errors and sharp interfaces between turbulent and non-turbulent regions exist.

A few previous studies have successfully utilized a high order approximation of the convective flux of linear RANS turbulence models in structured grid-based flow solvers [2,3], and even in Reynolds stress transport models [4,5]. However, the use of a second-order, or a higher order accuracy for the approximation of the turbulence model equations convective flux in an unstructured grid-based flow solver is very rare [6,7]. Some progress was achieved by the author in designing a robust second order scheme for the turbulence model equations using unstructured grids [8]. It was found that a monotone discretization of the convective flux of the turbulence model alone may have a dramatic effect on the convergence characteristics of the governing equations. Specifically, the limiter that is applied to the second-order reconstruction of the turbulence model primitive variables vector plays a key role in the convergence characteristics of the flow solver.

The aim of the present work is to propose a modified two-equation turbulence model with a reduced sensitivity to the limiter type. The motivation is to specifically design the turbulence model for robust computations on unstructured grids. The main idea is to use a k-ω model (where k is the turbulent kinetic energy and ω is the specific dissipation rate of turbulent kinetic energy), specifically the model developed by Kok [9] (also known as the TNT model) as the baseline model. The transformed model, denoted q-s, is obtained by using a square root transformation to k and ω, namely $q = \sqrt{k}$ and $s = \sqrt{\omega}$. It is expected that this transformation will reduce the numerical sensitivity, especially at near-wall regions. The idea of using a square root transformation is not new. For example, the q-ω model, developed by Coakly and Huang [10], the k-$\sqrt{\omega}$ model, proposed by Jiang et al. [11],

and the q-l model, developed by Goldberg [12], all use the square root transformation technique. The present model mainly differs from these models by fully retaining all of the new terms that emerge from the transformation. Therefore, the transformed model should reproduce the original model performance but with improved convergence and stability characteristics.

2. Governing equations

In the present work, the flow is modeled by the compressible Reynolds averaged Navier–Stokes equations. The Reynolds stress tensor is modeled via the Boussinesq approximation using two-equation turbulence model, i.e, the k-ω or the q-s models.

2.1. Mean-flow equations

In a compact vector form, the mean-flow equations may be expressed in a Cartesian coordinate system as:

$$\frac{\partial \boldsymbol{V}}{\partial \tau} + \frac{\partial (\boldsymbol{F}_j^c - \boldsymbol{F}_j^d)}{\partial x_j} = 0 \tag{1}$$

where τ denotes the time and $x_i = [x, y, z]$ denotes the Cartesian coordinates. The vectors $\boldsymbol{V}$, $\boldsymbol{F}_j^c$ and $\boldsymbol{F}_j^d$, represent the mean-flow dependent variables, the inviscid flux, and the diffusive flux, respectively. These are given as:

$$\boldsymbol{V} = \begin{bmatrix} \rho \\ \rho u_i \\ E \end{bmatrix}, \quad \boldsymbol{F}_j^c = \begin{bmatrix} \rho u_j \\ \rho u_j u_i + p\delta_{ij} \\ \rho u_j H \end{bmatrix}, \quad \boldsymbol{F}_j^d = \begin{bmatrix} 0 \\ \tau_{ij} + \Re_{ij} \\ \beta_j \end{bmatrix} \tag{2}$$

where ρ is the fluid density. The Cartesian velocity vector components are denoted by $u_i = [u, v, w]$, and the total energy is denoted by E. The pressure is denoted by p and $H = (E + p)/\rho$ is the total enthalpy. The quantities τ_{ij} and $\Re_{ij}$ are the components of the viscous stress and Reynolds-stress tensors, respectively. Applying the Boussinesq approximation, the Reynolds stress tensor takes the form:

$$\Re_{ij} = 2\mu_t \left(S_{ij} - \frac{1}{3} \frac{\partial u_k}{\partial x_k} \delta_{ij} \right) - \frac{2}{3} \rho k \delta_{ij} \tag{3}$$

where k denotes the turbulence kinetic energy, δ_{ij} is the Kronecker delta function and S_{ij} is the strain tensor:

$$S_{ij} = \frac{1}{2} \left(\frac{\partial u_i}{\partial x_j} + \frac{\partial u_j}{\partial x_i} \right) \tag{4}$$

The terms β_j are given by:

$$\beta_j = u \left(\tau_{j1} + \Re_{j1} \right) + v \left(\tau_{j2} + \Re_{j2} \right) + w \left(\tau_{j3} + \Re_{j3} \right) - q_j - (q_t)_j \tag{5}$$

where q_j and q_{t_j} are the molecular and turbulent heat fluxes, respectively, and are modeled using Fourier's law as:

$$q_j = -\kappa \frac{\partial T}{\partial x_j} \tag{6}$$

$$q_{t_j} = -\kappa_t \frac{\partial T}{\partial x_j} \tag{7}$$

The temperature is denoted by T and $\kappa = c_p\mu/Pr$ and $\kappa_t = c_p\mu_t/Pr_t$ are the molecular and turbulent heat conductivity coefficients, respectively. The term μ denotes the molecular viscosity, calculated using Sutherland's law. The term μ_t denotes the turbulent viscosity. The term c_p is the specific heat capacity at constant pressure, while $Pr = 0.72$ and $Pr_t = 0.9$ are the molecular and turbulent Prandtl numbers, respectively. The mean-flow equations are closed using the equation of state for a perfect gas, given by:

$$p = (\gamma - 1) \left[E - \frac{1}{2}\rho \left(u^2 + v^2 + w^2 \right) \right] \tag{8}$$

where γ is the ratio of the specific heat (c_p/c_v), set to $\gamma = 1.4$. Note that the contribution of the turbulent diffusion to the total energy transport equation is neglected, as well as the contribution of the turbulent kinetic energy to the total energy.

2.2. Two-equation turbulence model

The proposed model is derived from the k-ω model (TNT model) developed by Kok [9]. The k-ω model may be presented in a compact vector form in Cartesian coordinates as follows:

$$\frac{\partial \boldsymbol{v}}{\partial \tau} + \frac{\partial (\boldsymbol{f}_j^c - \boldsymbol{f}_j^d)}{\partial x_j} = \boldsymbol{S}_{k\omega} \tag{9}$$

where $\boldsymbol{v} = [\rho k, \rho\omega]^T$ is the turbulence model dependent variables vector. The turbulence model convective flux vector, $\boldsymbol{f}_j^c$, and diffusive flux vector, $\boldsymbol{f}_j^d$, are given by

$$\boldsymbol{f}_j^c = \begin{bmatrix} \rho k u_j \\ \rho\omega u_j \end{bmatrix}, \quad \boldsymbol{f}_j^d = \begin{bmatrix} \Gamma_k \frac{\partial k}{\partial x_j} \\ \Gamma_\omega \frac{\partial \omega}{\partial x_j} \end{bmatrix} \tag{10}$$

The turbulence model source vector, $\boldsymbol{S}_{k\omega}$, is given as:

$$\boldsymbol{S}_{k\omega} = \begin{bmatrix} P_k - \beta_k \rho\omega k \\ \alpha_\omega \frac{\omega}{k} P_k - \beta_\omega \rho\omega^2 + \Gamma_d \max\left(\frac{\partial k}{\partial x_i} \frac{\partial \omega}{\partial x_i}, 0 \right) \end{bmatrix} \tag{11}$$

where P_k, defined as $P_k = \Re_{ij}\frac{\partial u_i}{\partial x_j}$, represents the production of the turbulent kinetic energy. The turbulence model diffusive coefficients, Γ_k, Γ_ω, and Γ_d, are defined as follows:

$$\Gamma_k = \mu + \sigma_k\mu_t, \quad \Gamma_\omega = \mu + \sigma_\omega\mu_t, \quad \Gamma_d = \sigma_d \frac{\rho}{\omega} \tag{12}$$

The constants of the model are given by:

$$\beta_k = 0.09, \quad \sigma_d = 0.5, \quad \alpha_\omega = 0.55316667, \quad \beta_\omega = 0.075,$$
$$\sigma_k = 2/3, \quad \sigma_\omega = 0.5 \tag{13}$$

Two-equation turbulence models may suffer from spurious overproduction of turbulent kinetic energy in certain regions. Although this phenomenon is known as the *stagnation point anomaly*, it usually appears in highly strained flows [13,14]. This anomaly results in the generation of excessive, large, *unrealistic* values of turbulent viscosity. The definition of *unrealistic* refers to values that cause the Reynolds stress tensor to violate realizability [15]. A realizability constraint that was developed by Mokhtarpoor and Heinz [16] was adopted as follows:

$$\mu_t = \rho k \min\left[\frac{1}{\omega}, \frac{c_R}{\Omega_s} \right] \tag{14}$$

where $\Omega_s = \sqrt{2S_{ij}S_{ij}}$ and c_R is a constant that is set to $c_R = \frac{23}{24\sqrt{3}}$. Note that the above realizability constraint is not a part of the original TNT model.

2.2.1. Derivation of the q-s model

Using the following definitions, $q = \sqrt{k}$ and $s = \sqrt{\omega}$, the q-s model is obtained as follows:

$$\frac{\partial \boldsymbol{v}}{\partial \tau} + \frac{\partial (\boldsymbol{f}_j^c - \boldsymbol{f}_j^d)}{\partial x_j} = \boldsymbol{S}_{qs} \tag{15}$$

where $\boldsymbol{v} = [\rho q, \rho s]^T$ is the turbulence model dependent variables vector. The turbulence model convective flux vector, $\boldsymbol{f}_j^c$, and diffusive flux vector, $\boldsymbol{f}_j^d$, are given by

$$\boldsymbol{f}_j^c = \begin{bmatrix} \rho q u_j \\ \rho s u_j \end{bmatrix}, \quad \boldsymbol{f}_j^d = \begin{bmatrix} \Gamma_k \frac{\partial q}{\partial x_j} \\ \Gamma_\omega \frac{\partial s}{\partial x_j} \end{bmatrix} \tag{16}$$

The turbulence model source vector, $\boldsymbol{S}_{qs}$, is given as:

$$\boldsymbol{S}_{qs} = \begin{bmatrix} \frac{P_k}{2q} - \frac{\beta_k}{2}\rho s^2 q + \Gamma_q \frac{\partial q}{\partial x_i} \frac{\partial q}{\partial x_i} \\ \frac{\alpha_\omega}{2} \frac{s}{q^2} P_k - \frac{\beta_\omega}{2}\rho s^3 + \Gamma_d \max\left(\frac{\partial q}{\partial x_i} \frac{\partial s}{\partial x_i}, 0 \right) + \Gamma_s \frac{\partial s}{\partial x_i} \frac{\partial s}{\partial x_i} \end{bmatrix} \tag{17}$$
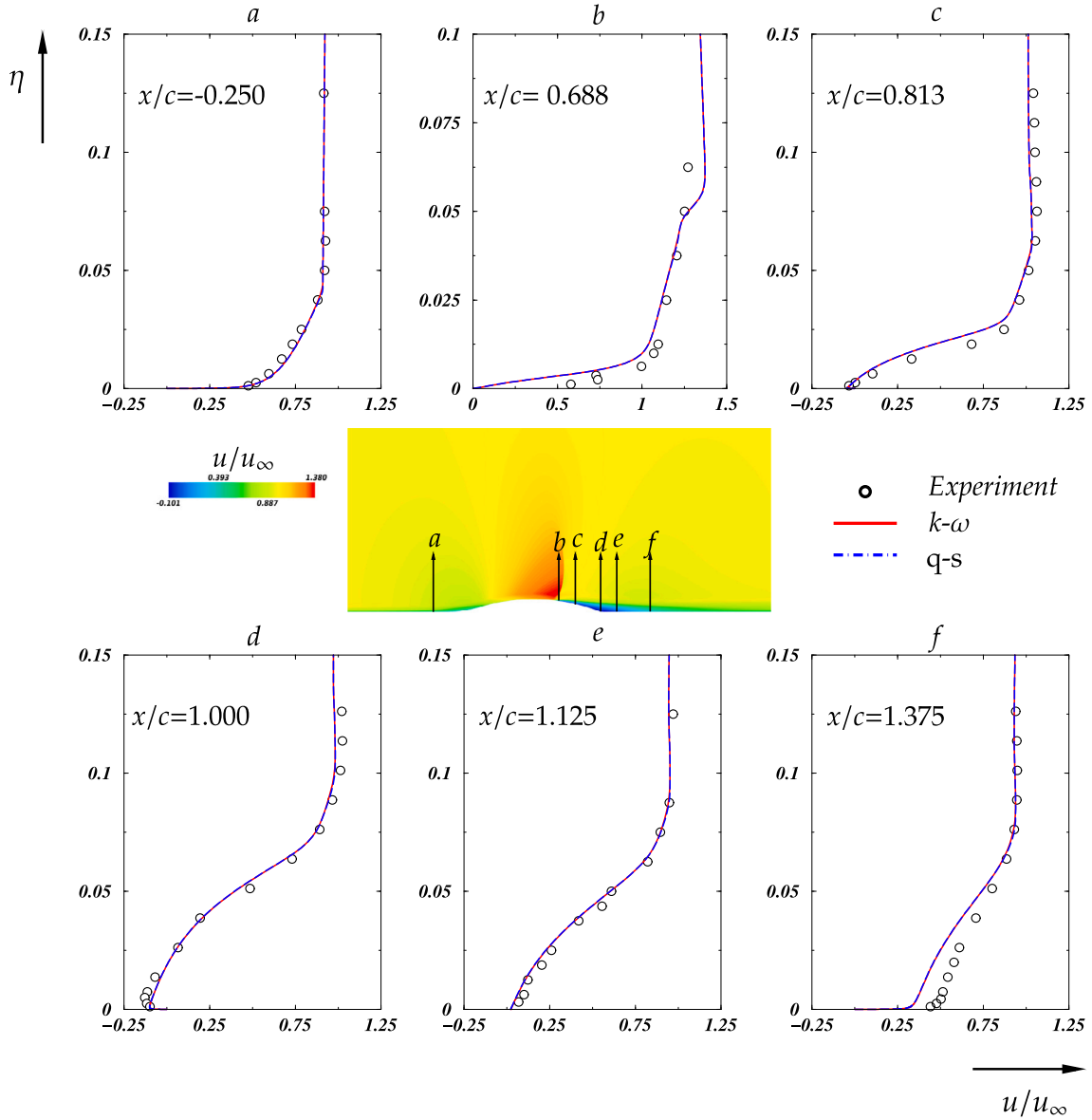
Fig. 1. Comparison of the normalized stream-wise velocity profiles at six stations over the axisymmetric bump.

The turbulence model diffusive coefficients, Γ_k, Γ_ω, and Γ_d, are defined as follows:

$$\Gamma_k = \mu + \sigma_k \mu_t, \quad \Gamma_\omega = \mu + \sigma_\omega \mu_t, \quad \Gamma_d = 2\sigma_d \mu_t \frac{1}{q}, \quad \Gamma_q = \Gamma_k \frac{1}{q}, \quad \Gamma_s = \Gamma_\omega \frac{1}{s}$$

$$(18)$$

The turbulent viscosity is calculated as:

$$\mu_t = \rho q^2 \min \left[\frac{1}{s^2}, \frac{c_R}{\Omega_s} \right] \tag{19}$$

The constants of the model remain the same as in the baseline *k-ω* model.

3. Numerical method

A conservative finite volume methodology to discretize the governing equations on unstructured grids is employed. The diffusive flux vector is discretized by employing a second-order central differencing method using a full viscous stencil. The cell face gradient of the primitive variables is approximated as suggested by Jawahar

and Kamath [17]. The mean-flow equations inviscid flux vector is approximated at the cell interface using the AUFSR+ scheme [18]. The turbulence model's inviscid flux vector is computed using the HLLC scheme [19]. The left and right state vectors of the convective flux are evaluated using second order accuracy and are obtained by linear reconstruction. A cell-wise gradient of the primitive variables is constructed using Green's theorem. Let the vector $\boldsymbol{W} = (W_m; m = 1, \dots 7)$ denote the primitive variables vector,

$$\boldsymbol{W} = \begin{cases} [\rho, u, v, w, p, k, \omega] & k - \omega \ model \\ [\rho, u, v, w, p, q, s] & q - s \ model \end{cases} \tag{20}$$

then the left and right primitive variables are reconstructed as follows:

$$(W_m)_L = (W_m)_i + (\psi_m)_i (\nabla W_m)_i \cdot \boldsymbol{d}_i^{ij} \tag{21a}$$

$$(W_m)_R = (W_m)_j + (\psi_m)_j (\nabla W_m)_j \cdot \boldsymbol{d}_j^{ij} \tag{21b}$$

where $\boldsymbol{d}_i^{ij}$ and $\boldsymbol{d}_j^{ij}$ are the distance vectors from the centers of cells i and j, respectively, to the mid-point of face ij. The term ψ_m is the cell limiter that is used to suppress oscillations in the solution.
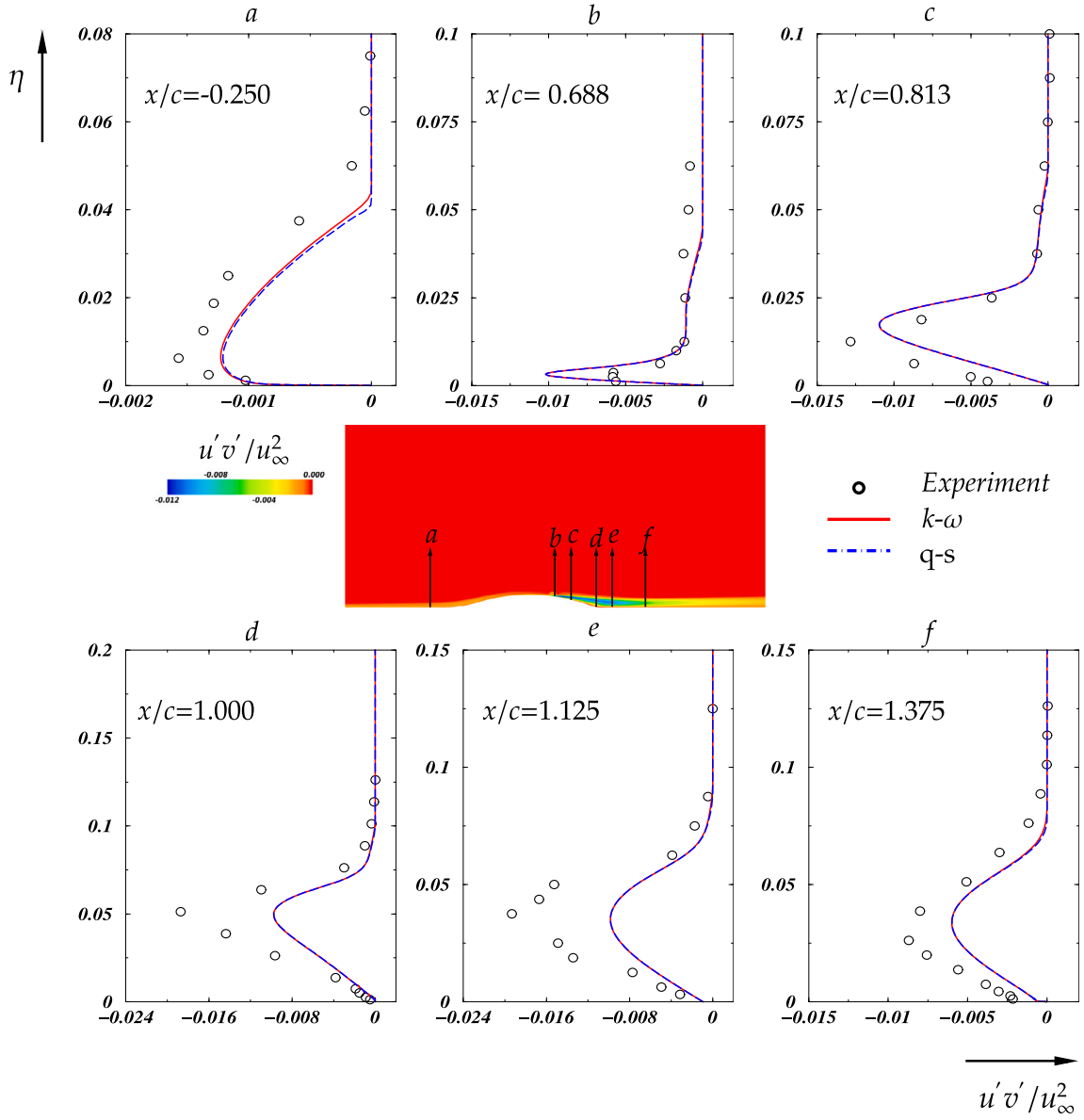
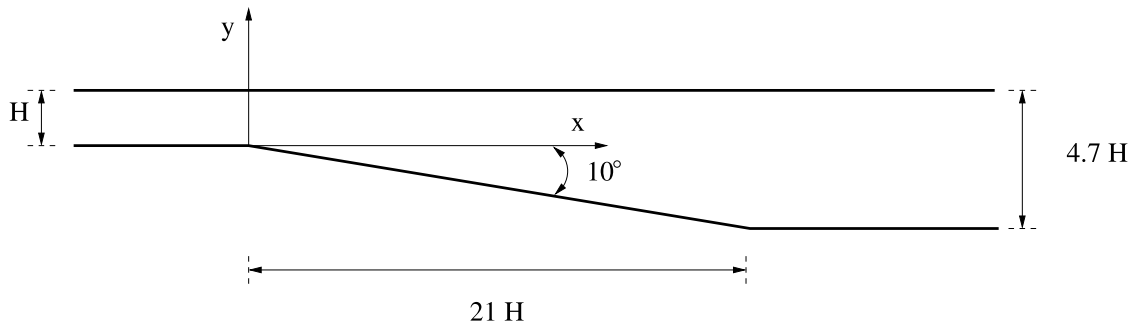**Fig. 2.** Comparison of shear stress component profiles at six stations over the axisymmetric bump.

Fig. 3. Schematic description of the plane asymmetric diffuser geometry.

Two limiters were used: the limiter developed by Venkatakrishnan [20] and the limiter developed by Park and Kim [21], also known as the *MLP-u2* limiter. The limiter developed by Park and Kim adopts the structure of the Venkatakrishnan limiter, however, it differs by the limiter arguments. The limiter function ψ is defined as follows:

$$\psi = \frac{1}{\Delta_-}\left[\frac{\left(\Delta_+^2 + \epsilon^2\right)\Delta_- + 2\Delta_-^2\Delta_+}{\Delta_+^2 + 2\Delta_-^2 + \Delta_-\Delta_+ + \epsilon^2}\right] \tag{22}$$
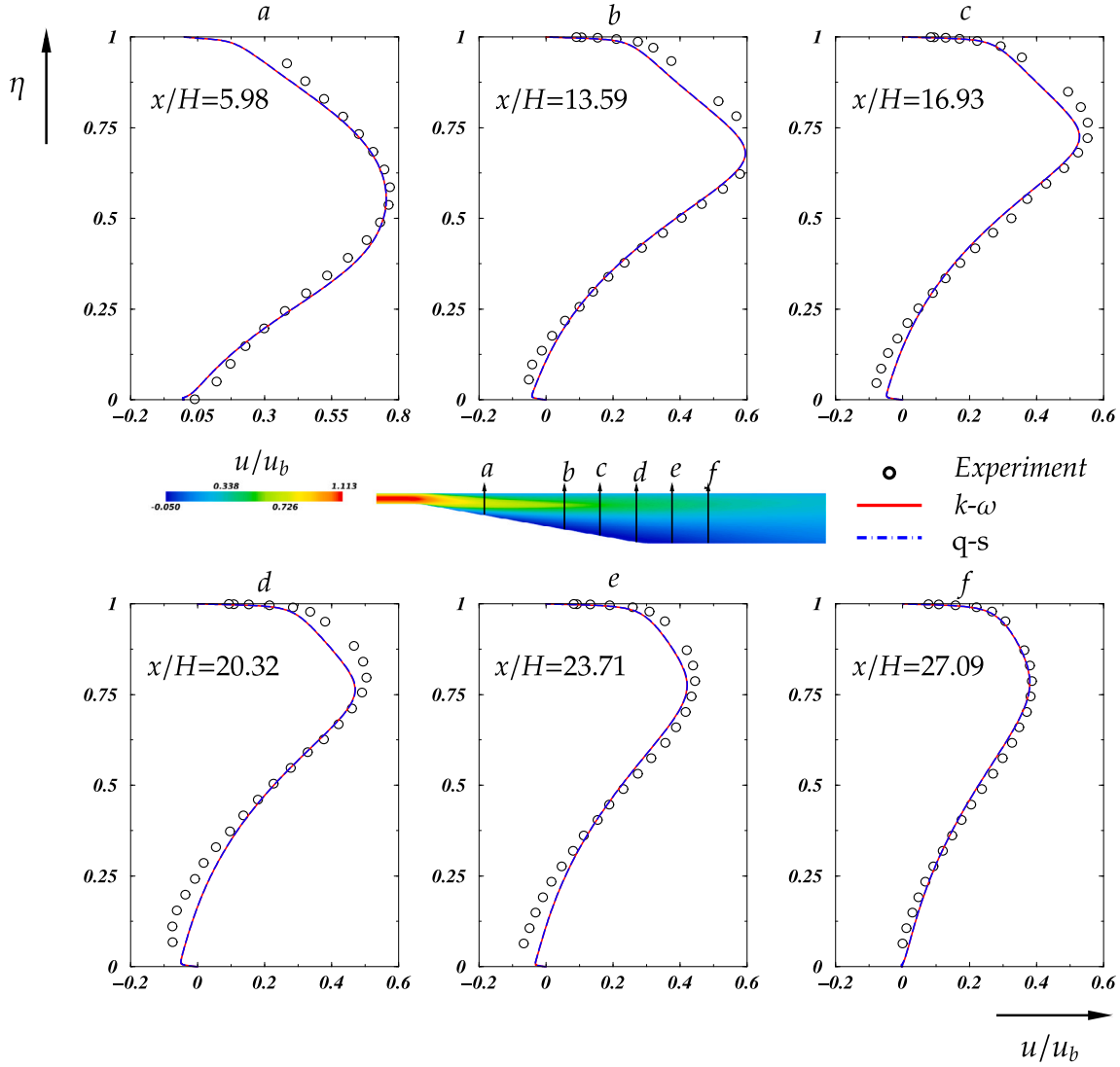
Fig. 4. Comparison of stream-wise velocity profiles at six stations along the separation region of the plane asymmetric diffuser.

where ϵ is a threshold parameter that distinguishes between a nearly smooth region and a fluctuating one. The specific definitions of Δ_+ and Δ_- are given in the original publications [20,21]. The threshold parameter ϵ is defined as follows:

$$\epsilon^2 = \begin{cases} \left(K_1 L_c\right)^3, & Venkatakrishnan \\ \dfrac{K_1}{1+\theta}\Delta_Q^2, \quad \theta = \dfrac{\Delta_Q}{K_2 L_c^{3/2}}, & MLP-u2 \end{cases} \tag{23}$$

where L_c is a characteristic cell length, taken in the present work as $L_c = V^{1/3}$, K_1 and K_2 are constants, and Δ_Q is defined as the maximum local flow variation. For the sake of simplicity, in the current work, the two MLP-$u2$ limiter constants are set as equal to one another. Experience indicates that the solution and the convergence of the mean flow equations are not very sensitive to the values of the constants, as long as they admit values in the order of unity $\sim \mathcal{O}(1)$. However, their values, when applied to turbulence model variables reconstruction, may be critical to the flow solver robustness. In a previous work [8], it was found that using the Venkatakrishnan limiter to the turbulence model variables results in serious convergence difficulties, regardless of the values of the limiter constant. On the other hand, using the MLP-$u2$ limiter, a stable solution could be obtained. However, in this case, low values of the constants (corresponds to the turbulence model variables) were required.

To study the influence of these constants on the convergence characteristics, especially of the turbulence model equations, separate constants are defined for each set of the governing equations, *i.e.*, the mean-flow equations set and the turbulence model equations set. Namely, K_{MF} represents the limiter constants applied to the mean-flow variables reconstruction. In a similar manner, K_{TM} represents the constant that is used for the turbulence model variables reconstruction.

Since the current work focuses on steady-state flows only, a first-order implicit backward Euler time integration method is utilized. Moreover, the implicit operator of the turbulence model is derived using the unconditionally positive-convergent (UPC) scheme [8,22,23]. To further enhance the implicit operator stability, the five-stage implicit Runge–Kutta scheme is employed [24].

It should be noted that the proposed variable substitution does not remove the singular behavior of ω at the wall. However, the square-root transformation is expected to numerically relieve this singular behavior at a cost of the emergence of additional source diffusion terms. This *shifting* of difficulties, was thoroughly discussed by Langer and Swanson [25]. Indeed, the numerical treatment of diffusion source terms in general is rarely addressed, as it does not easily lend itself to a stable numerical scheme. However, a stabilized implicit method for the diffusion source terms was recently proposed by the current author [26]. This method is adopted in current work.
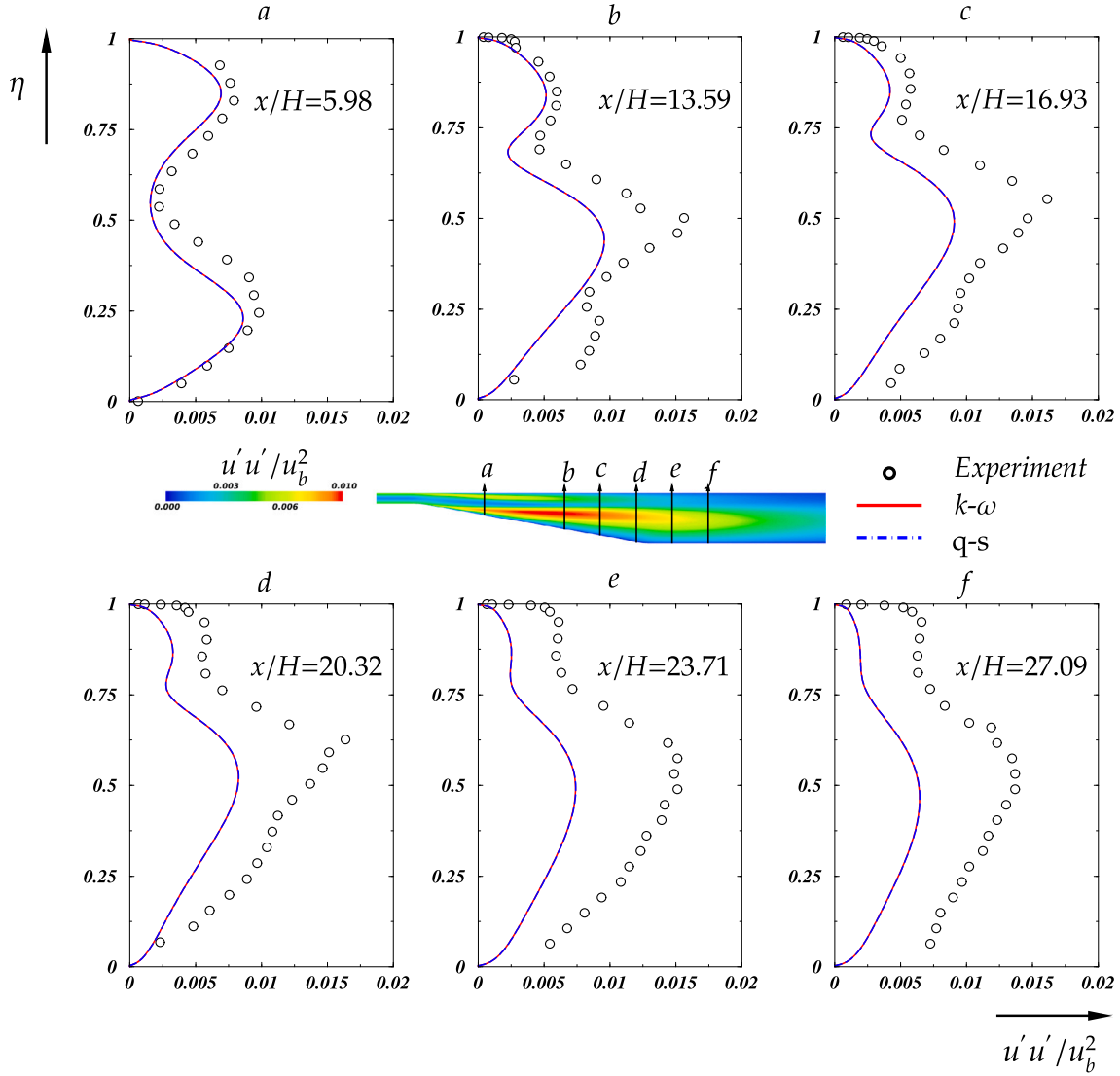
Fig. 5. Comparison of normal-Reynolds stress profiles at six stations along the separation region of the plane asymmetric diffuser.

3.1. Realizability of the turbulence model

Realizability in the broad sense refers to the ability of the governing equations and the numerical scheme to be physically sound. One example already mentioned earlier is the realizability of the Reynolds stress tensor. Another realizability measure is the positivity of the turbulence model variables. In the present work, the positivity of the turbulence model variables is guaranteed thanks to the use of the UPC scheme. The UPC scheme preserves positivity for any time step and for any low values, down to the computer machine minimum normalized positive value ($DBL\_MIN = 2.225E - 308$).

The turbulence model variables may admit extremely low values. This situation may be due to the interaction between several factors, such as the limiter, the time integration method, and the discretization method. For example, a non-monotonic solution may result in a spurious solution which in turn results in a strong decay of the turbulence model variables. Using the k-ω model with the Venkatakrishnan limiter (that is applied to the reconstruction of k and ω) usually results in extremely low values of k and ω, possibly down to the DBL_MIN. To prevent the solution from reaching such meaningless low values, artificially set low limit values are utilized for both k and ω. These limits are set to 1×10^{-20} of their freestream (inflow) values. Using the MLP-$u2$ limiter, this limit is activated only for k, and only when the

limiter constant K_{TM} is set to a relatively high value of $K_{TM} = 5$ (namely a low dissipation scheme). Note that the positivity of the turbulence model variables is monitored and verified prior to enforcing these extremely low limits.

On the other hand, using the q-s turbulence model, no artificially low limit values are used nor any other bounds are required. This is regardless of the limiter type and its constants.

4. Numerical examples

Four test cases are simulated and examined. The aim of the tests is to study the iterative convergence properties of the q-s model, specifically its sensitivity to the limiter type. Beginning with the transonic flow over an axisymmetric bump, followed by two-dimensional flow in an asymmetric plane diffuser. These two cases were chosen to examine the flow prediction similarity between the baseline k-ω model and the q-s model. The other two cases are the NHLP-2D multi-element airfoil at a high angle of attack, and the transonic flow about the NACA0012 airfoil.

Several general remarks and definitions should be made:

- The initial solutions of the mean-flow equations and of the turbulence model equations are uniform and are based on free-stream values.
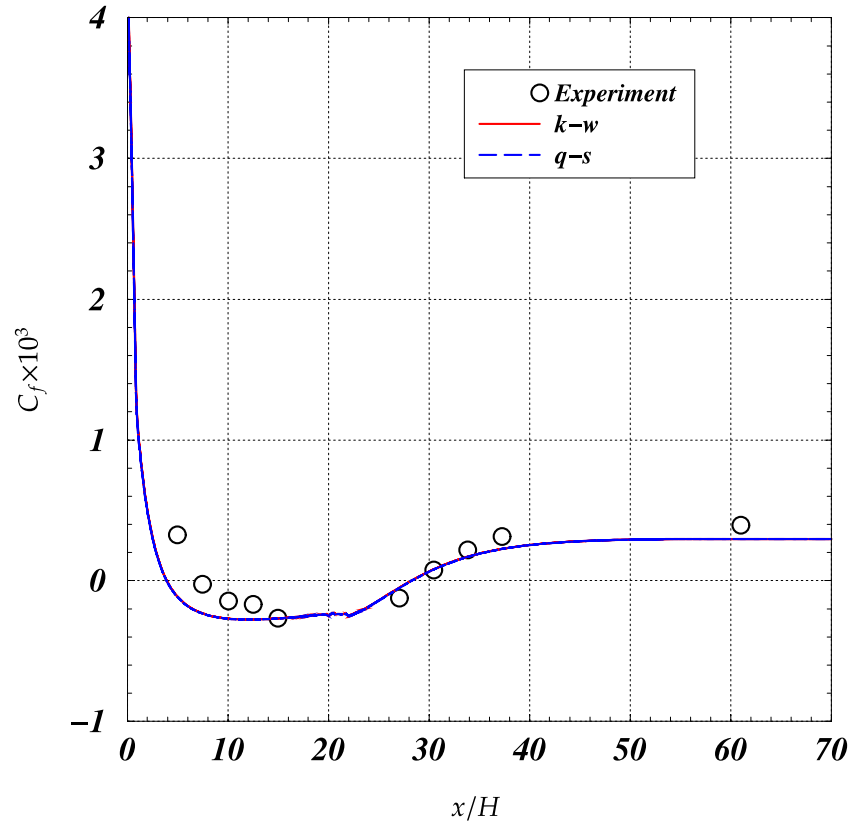
Fig. 6. Comparison of the lower wall shear stress coefficient of the plane asymmetric diffuser.
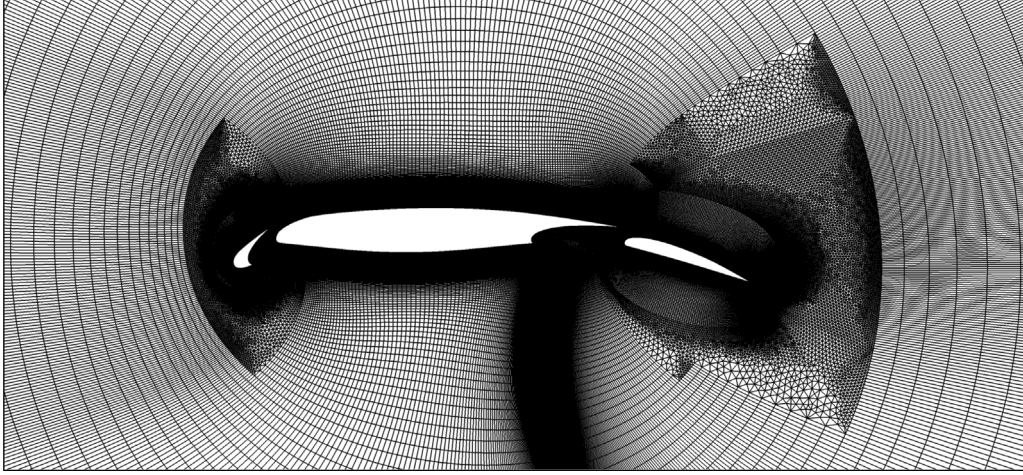

Fig. 7. The multi-element NHLP-2D airfoil unstructured grid.

- An infinite CFL number was used for the turbulence model equations (the artificial time derivative is dropped). All subsequent CFL numbers that are mentioned herein refer to the mean-flow equations only.

- Let the vectors $\boldsymbol{R}$ and $\boldsymbol{r}$ signify the discrete residuals of the mean-flow equations and of the turbulence model equations, respectively. Iterative convergence is measured by examining the relative drop (in orders of magnitude) of the second norm of the residual vector with respect to the initial residual. The iterative convergence of the mean-flow equations and of the turbulence model equations is denoted by $e_{MF} = \log(\|\boldsymbol{R}\|_2/\|\boldsymbol{R}_0\|_2)$ and $e_{TM} = \log(\|\boldsymbol{r}\|_2/\|\boldsymbol{r}_0\|_2)$, respectively.

- All simulations are conducted with the mean-flow variables limiter constant K_{MF} set to $K_{MF} = 5$.

4.1. Boundary conditions

Characteristic boundary conditions that are based on the Riemann invariants are used for the mean-flow equations at the far-field boundaries. On solid walls, an adiabatic, no-slip boundary condition is applied. The turbulent kinetic energy, k, and its square root q are set to zero on solid walls ($q_{wall} = \sqrt{k_{wall}}$). The free-stream turbulent kinetic energy is evaluated according to the relation $k_\infty = \frac{3}{2}[(Tu)^2(u_\infty^2 + v_\infty^2 + w_\infty^2)]$, where Tu represents the turbulence intensity ($q_\infty = \sqrt{k_\infty}$). The turbulent specific dissipation rate at the wall is specified in accordance
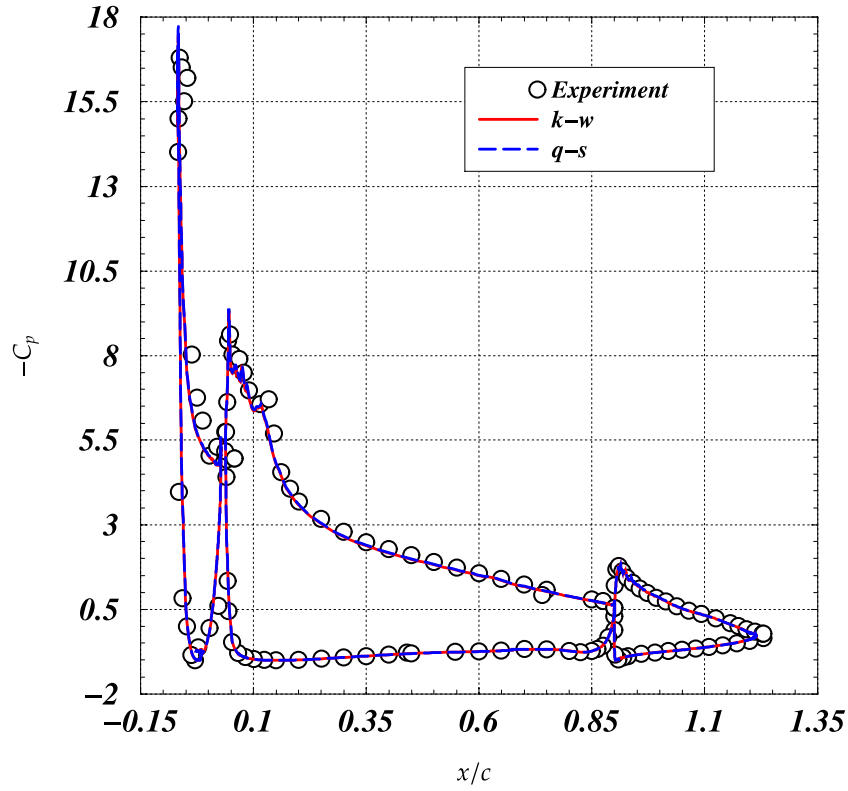
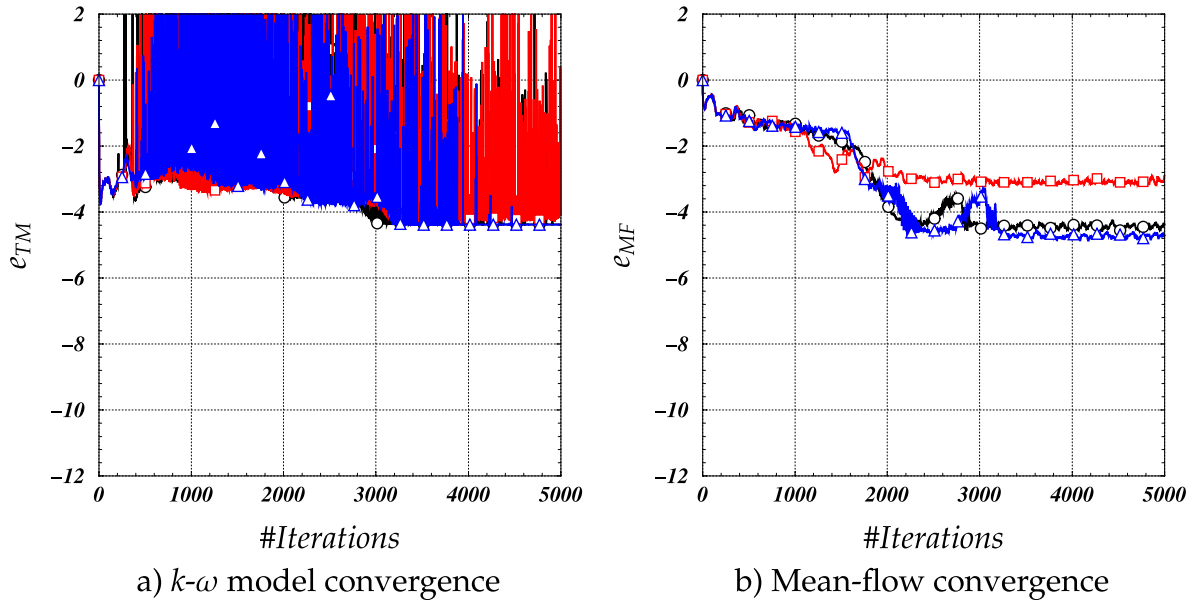**Fig. 8.** Comparison of the surface pressure coefficient distributions about the NHLP-2D airfoil.

a) k-ω model convergence

b) Mean-flow convergence

Fig. 9. Convergence histories from flow simulations about the NHLP-2D airfoil at $\alpha = 20.18°$ using the k-ω model with the Venkatakrishnan limiter; $K_{TM} = 0.5$: —△——△—, $K_{TM} = 2$: —□——□—, $K_{TM} = 5$: —○——○—.

with the work by Menter [27], and is set to $\omega_{wall} = 10\frac{6\mu}{\rho\beta_\omega d_1}$. Here, d_1 is the wall distance to the first cell center adjacent to the wall. In a similar manner, the wall boundary condition of s is specified as $s_{wall} = 10\sqrt{\frac{6\mu}{\rho\beta_\omega d_1}}$.

4.1.1. Axisymmetric transonic bump

The transonic flow over an axisymmetric bump is a complex test case, designed for the validation of turbulence models. It was experimentally investigated by Bachalo and Johnson [28]. A compression

shock develops, interacting with the boundary layer, thus inducing flow separation over the rear part of the bump. The flow reattaches further downstream. To accurately predict the shock location and the separation point, the turbulence model must adequately resolve the up-stream boundary layer which includes favorable and adverse pressure gradients. The position of flow reattachment is also highly dependent on the turbulent shear stresses that develop in the separated shear layer. Experimental data was recorded at a free-stream Mach number of M_∞ = 0.875 and a Reynolds number of $Re_c = 2.763 \cdot 10^6$ (based on the chord
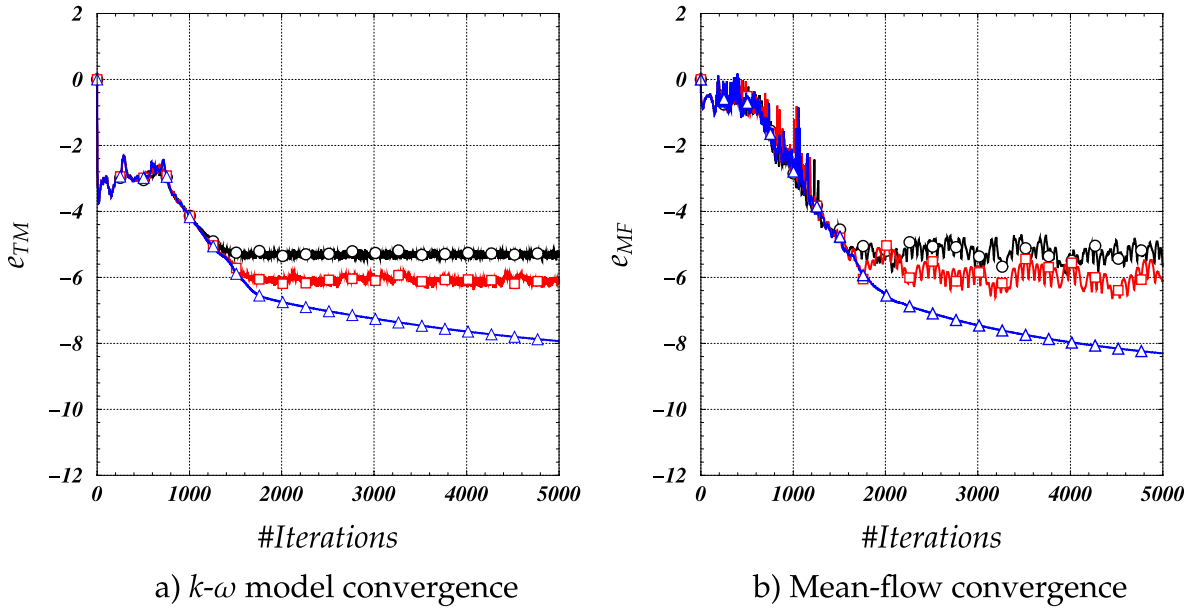
Fig. 10. Convergence histories from flow simulations about the NHLP-2D airfoil at $\alpha = 20.18°$ using the k-ω model with the *MLP-u2* limiter; $K_{TM} = 0.5$: —△——△—, $K_{TM} = 2$: —□——□—, $K_{TM} = 5$: —○——○—.

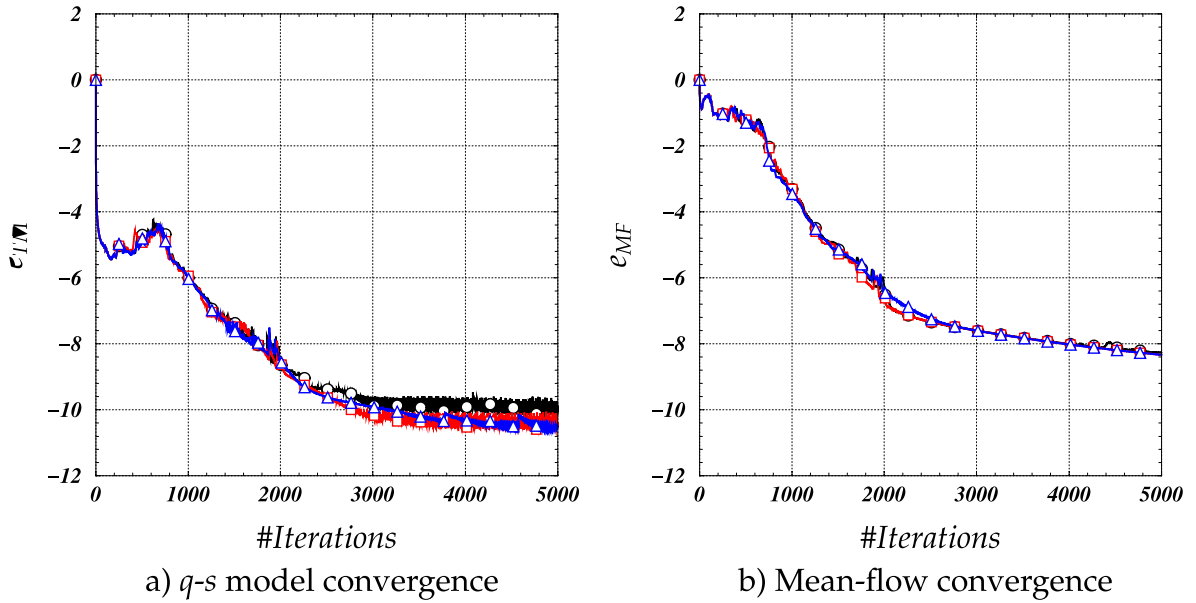**Fig. 11.** Convergence histories from flow simulations about the NHLP-2D airfoil at $\alpha = 20.18°$ using the q-s model with the Venkatakrishnan limiter; $K_{TM} = 0.5$: —△——△—, $K_{TM} = 2$: —□——□—, $K_{TM} = 5$: —○——○—.

length of the bump, denoted by c). The bump is located between $0 < x/c < 1$, so that its crest is located at $x/c = 0.5$. Numerical simulations are carried out using an axisymmetric computational structured grid that is provided on the TMR website [29]. The dimensions are 721 × 321 × 2 (stream-wise × wall-normal × circumferential points). The first grid point neighboring the wall is placed at a distance of 8×10^{-6} of the bump length, corresponding to a value of y_1^+ lower than 0.5. Based on the TMR practice, the free-stream turbulence intensity and the normalized free-stream turbulent viscosity, μ_t/μ, are set to 0.01% and 0.01, respectively. The simulations are conducted using both turbulence models (k-ω and q-s) and the *MLP-u2* limiter with $K_{TM} = 5$.

A comparison between the measured [28] and the computed normalized stream-wise velocity at six stations along the axisymmetric bump are shown in Fig. 1 (η denotes the vertical distance from the surface). Overall, the results obtained from the two turbulence models

are indistinguishable, as expected. Upstream of the bump, at $x/c = -0.25$, a good agreement with experimental data is obtained with both turbulence models. At $x/c = 0.688$, located between the experimental shock position and the separation onset point, certain deviations may be observed. At positions $x/c = 0.813$ and $x/c = 1.0$, located within the experimentally observed separation bubble, the computational results are in good agreement with the measurements. Outside the separation bubble, at $x/c = 1.125$, located past the experimental reattachment point, a good agreement is also obtained. Further downstream, at $x/c = 1.375$, a noticeable discrepancy between the computational results and the experimental data is observed, especially near the wall.

Similar to Fig. 1, a comparison of the normalized shear stress is shown in Fig. 2. While the agreement of the computed results with the experimental data at the first three stations is reasonable, the agreement is less satisfactory at the three stations downstream. With the
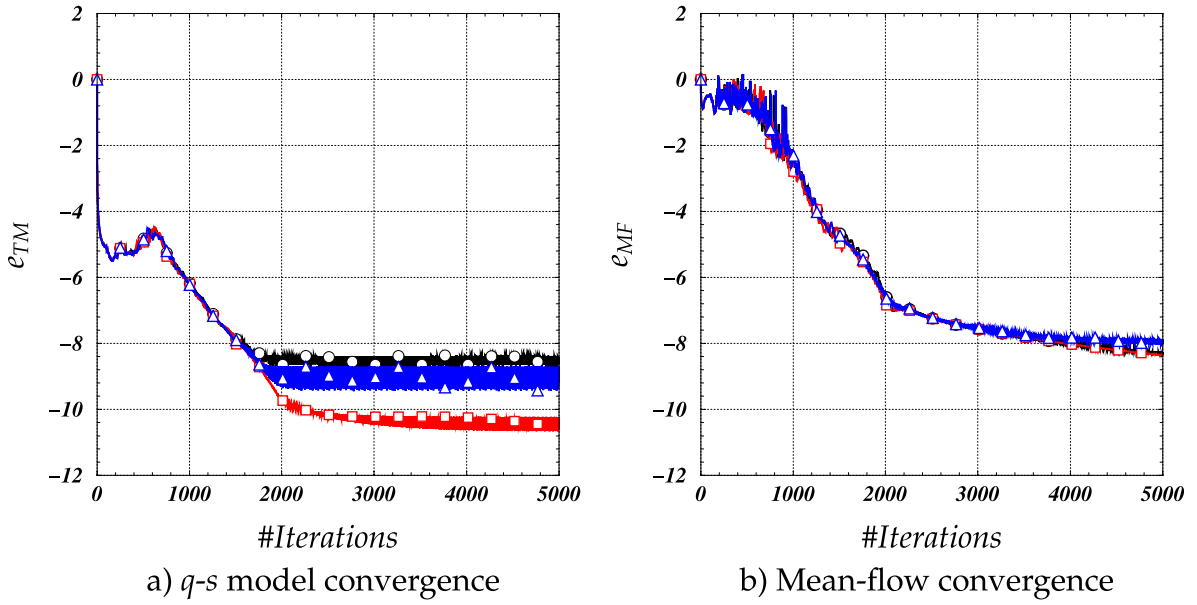
Fig. 12. Convergence histories from flow simulations about the NHLP-2D airfoil at $\alpha = 20.18°$ using the q-s model with the *MLP-u2* limiter; $K_{TM} = 0.5$: △——△——, $K_{TM} = 2$: □——□——, $K_{TM} = 5$: ○——○——.
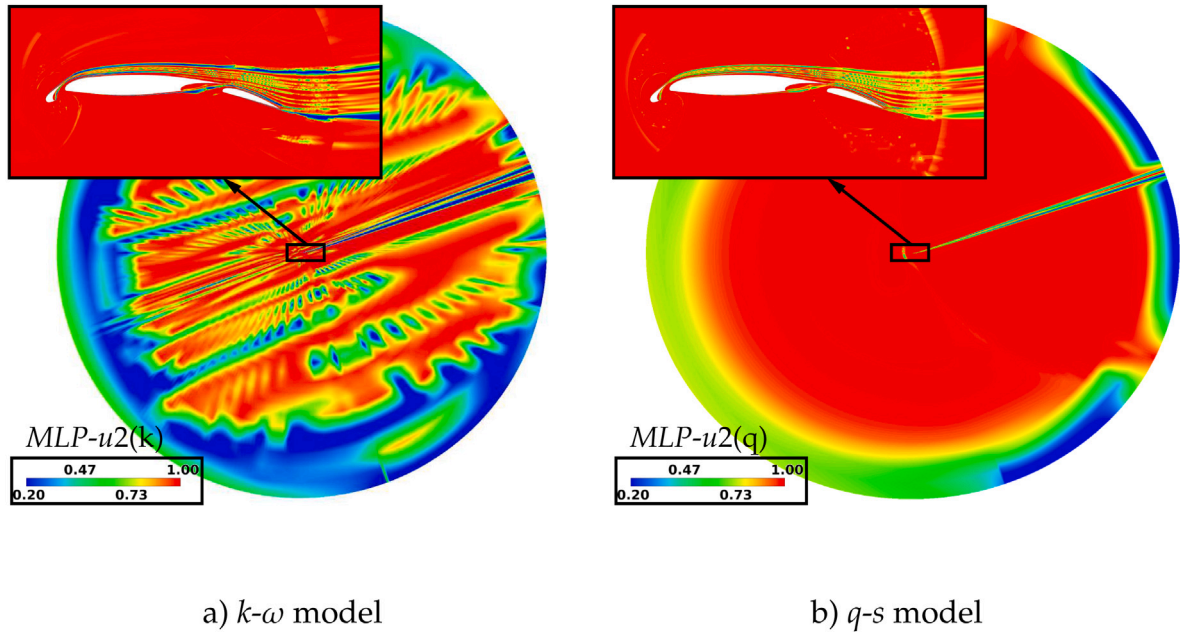

Fig. 13. Comparison of the *MLP-u2* limiter ($K_{TM} = 2$) distribution from flow simulations about the NHLP-2D airfoil.

exception of the minor difference at the first station, the results from the two models are indistinguishable. These models overlapping results indicate that the transformed model does not hamper the conservation of the baseline model equations.

4.1.2. Asymmetric plane diffuser

Computations of the steady turbulent flow through a plane asymmetric diffuser, schematically shown in Fig. 3, have been conducted. The flow in an asymmetric plane diffuser is difficult to predict. This is due to the presence of flow separation and reattachment within a confined domain, where adverse pressure gradients are quite dominant. This is especially difficult because the diffuser's upstream and downstream bottom inclined wall corners were rounded to prevent separation at these corners. Internal turbulent flow simulations of geometries where separation is not ruled by sharp corners is very

challenging, particularly the separation point location and the extent of the recirculation region.

The long inlet channel (110 times the channel's height, H) is followed by the diffuser with an opening angle of 10° of the bottom wall with an expansion ratio of 4.7. The outlet boundary is placed at the position of $x = 100H$. The plane asymmetric diffuser geometry was selected according to the experimental study performed by Buice and Eaton [30]. In the current work, the inlet Mach number is set to $M_b = 0.1$ and the reference Reynolds number, which is based on the channel height and the inlet velocity, is $Re_b = 2 \times 10^4$. The free-stream turbulence intensity and the normalized free-stream turbulent viscosity, μ_t/μ, are set to 0.05% and 0.01, respectively. The computational structured grid has the dimension of 805×307 where the first grid point neighboring the walls is placed at a distance of $2 \times 10^{-4}H$, resulting in a value of y_1^+ lower than 0.48. The *MLP-u2* limiter is
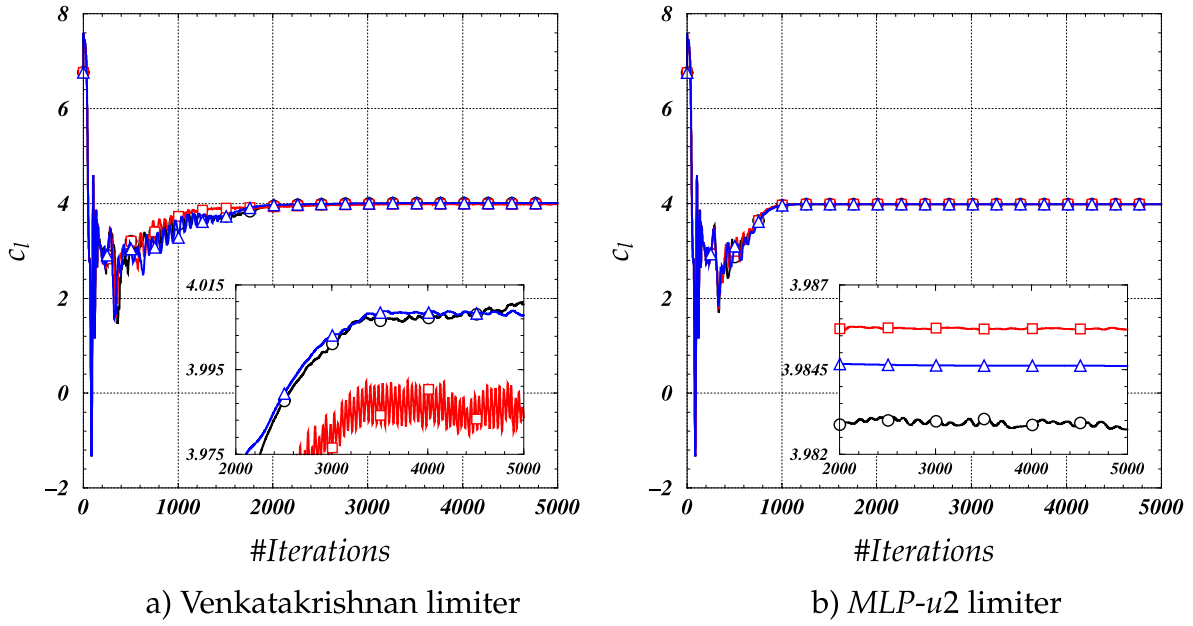
Fig. 14. Lift coefficient histories from flow simulations about the NHLP-2D airfoil at $\alpha = 20.18°$ using the k-ω model; $K_{TM} = 0.5$: —△——△—, $K_{TM} = 2$: —□——□—, $K_{TM} = 5$: —○——○—.
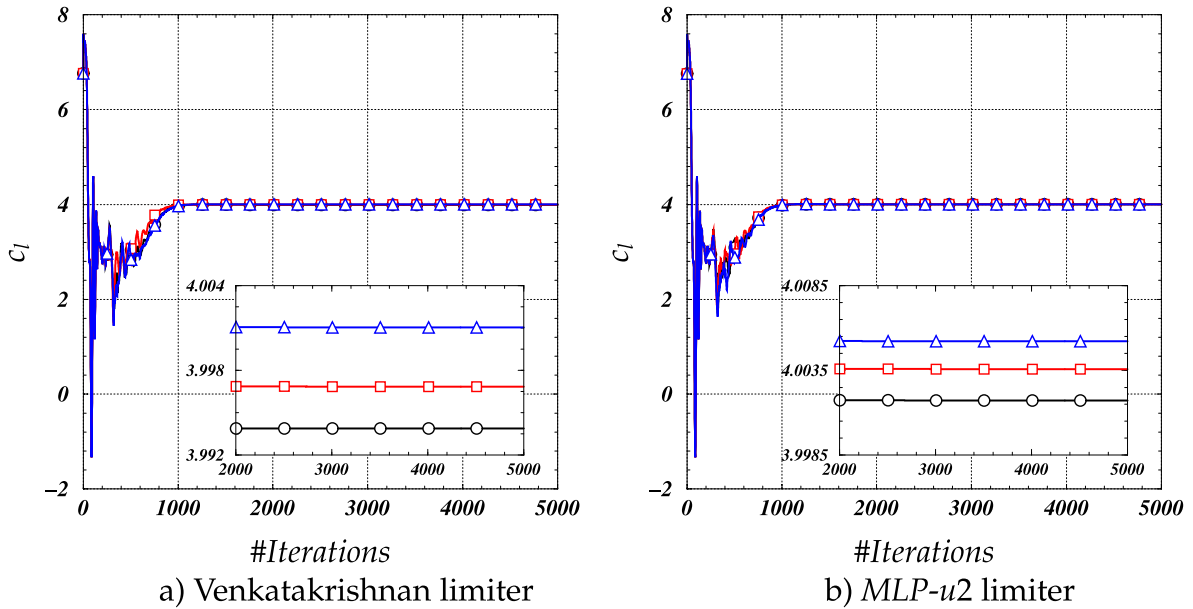

Fig. 15. Lift coefficient histories from flow simulations about the NHLP-2D airfoil at $\alpha = 20.18°$ using the q-s model; $K_{TM} = 0.5$: —△——△—, $K_{TM} = 2$: —□——□—, $K_{TM} = 5$: —○——○—.

utilized with $K_{TM} = 5$. A comparison of the calculated stream-wise velocity profile and the experimental data at six stations along the separation region is shown in Fig. 4. The computed results are in good agreement with the experimental data. The computed reattachment position is at $x/H = 28.4$, which is in a good agreement with the experiment [30] position of $x/H = 28.9$. Similar to the previous case of the axisymmetric transonic bump, the results obtained from the two turbulence models are indistinguishable.

Fig. 5 shows a comparison of the normalized Reynolds shear stress between computed results and experimental data. The computed stresses strongly underestimate the measured data. This is likely due to the use of a linear-eddy viscosity model. It was shown by Gerolymos et al. [31] that only advanced Reynolds stress models are capable of accurately capturing the Reynolds stresses. Another measure that

is used to further highlight the flow prediction of the two models is the wall shear stress coefficient (skin friction coefficient). Fig. 6 shows a comparison of the lower wall shear stress coefficient between computed results and experimental data. Both models predicted an early separation compared to the experiments. However, the overall agreement with the experimental results is very reasonable, and, as expected, the computed results overlap each other.

4.1.3. The NHLP-2D multi-element airfoil

The takeoff configuration of the NHLP-2D multi-element airfoil is chosen in the present work. In this configuration, the slat deflection is $\delta_s = 25°$ and the flap deflection is $\delta_f = 20°$. There are two different ways of defining the configuration: the vertical sense, as defined in the experiment [32], and the orthogonal sense, as adopted by most
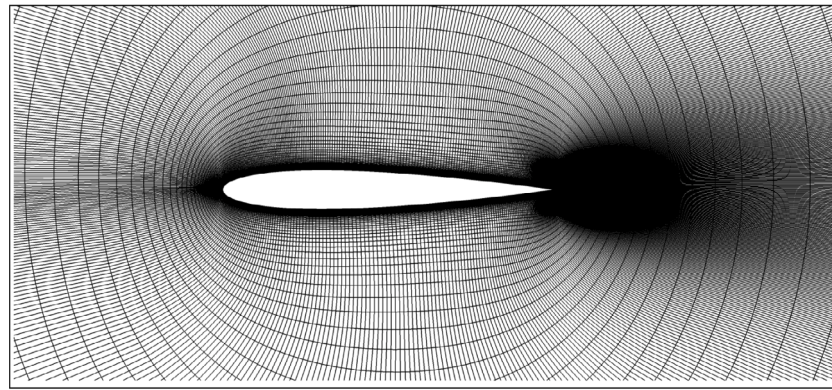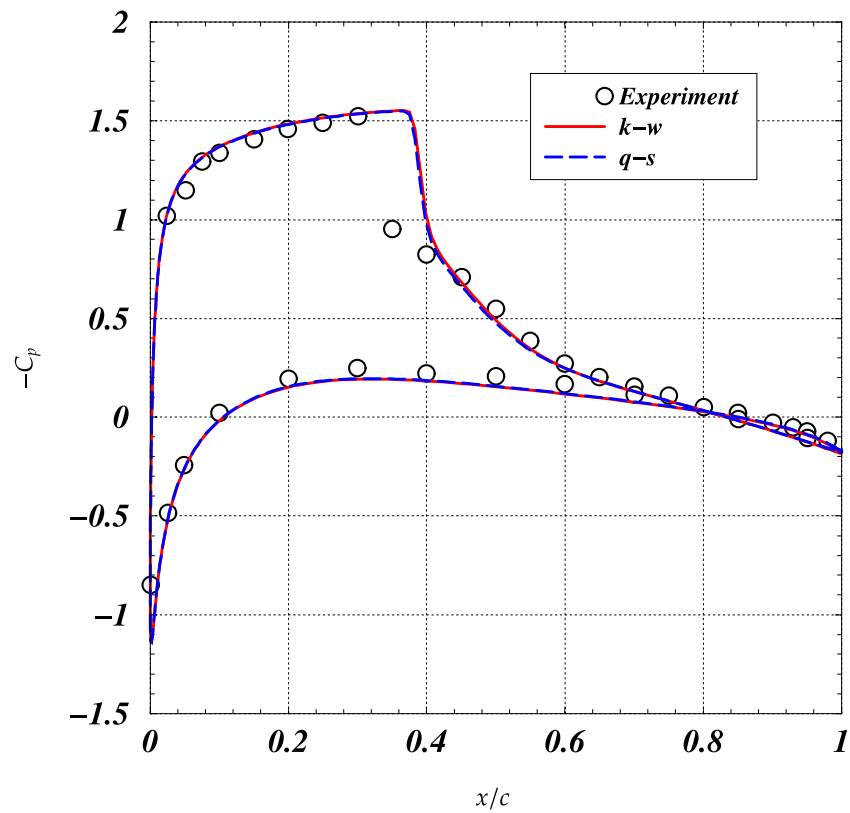
a) Structured grid
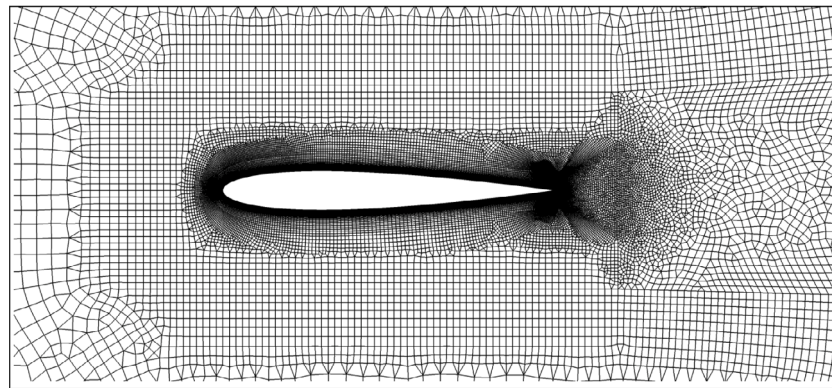
b) Unstructured grid

Fig. 16. The structured and unstructured grids about the NACA0012 airfoil.

Fig. 17. Comparison of the surface pressure coefficient distributions about the NACA0012 airfoil using the *MLP*-$u2$ limiter ($K_{TM} = 0.5$).
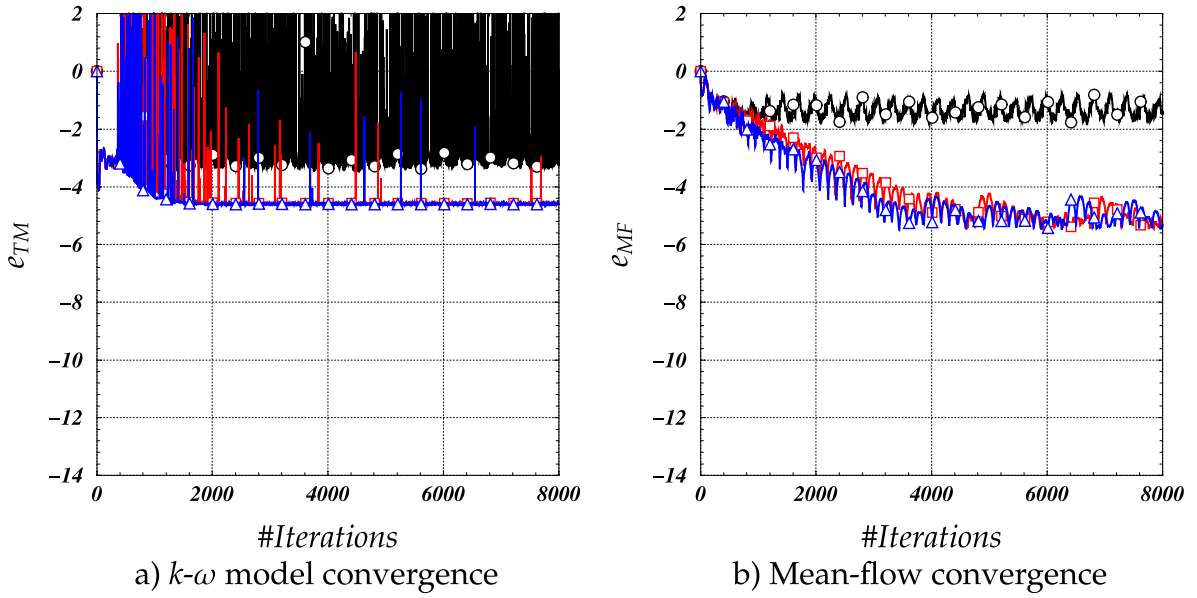
a) k-ω model convergence b) Mean-flow convergence

Fig. 18. Convergence histories from flow simulations about the NACA0012 airfoil with the unstructured grid using the k-ω model and the Venkatakrishnan limiter; $K_{TM} = 0.5$: —△——△—, $K_{TM} = 2$: —□——□—, $K_{TM} = 5$: —○——○—.

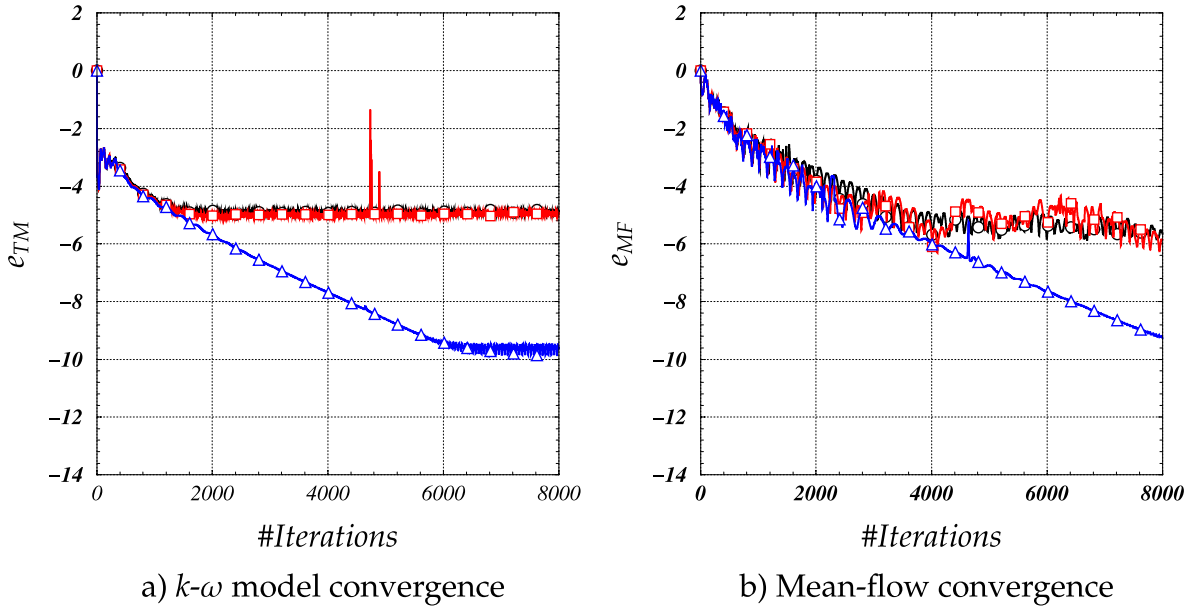a) k-ω model convergence b) Mean-flow convergence

Fig. 19. Convergence histories from flow simulations about the NACA0012 airfoil with the unstructured grid using the k-ω model and the MLP-u2 limiter; $K_{TM} = 0.5$: —△——△—, $K_{TM} = 2$: —□——□—, $K_{TM} = 5$: —○——○—.

researchers [33]. The current paper adopts the definition of the original experiment. Due to grid generation considerations, it is a common practice to sharpen the trailing edges of the three elements. In contrast, the exact experimental geometry is reproduced in the current work, and the trailing edges are of a finite thickness. The computational mesh is an unstructured grid composed of mixed-type elements, with approximately 294,000 cells (see Fig. 7). The center of the first cell neighboring the wall is located at a distance of 2.5×10^{-6} of the airfoil chord, from the airfoil surface (corresponds to a value of y_1^+ lower than 1.38). The computational domain extends up to approximately 230 airfoil chord lengths. The flow conditions are chosen to match those of the experiments. The free-stream Mach number is set to $M_\infty = 0.197$, the Reynolds number is set to $Re_\infty = 3.52 \times 10^6$, and the angle of attack is set to $\alpha = 20.18°$. The free-stream turbulence intensity and the normalized free-stream turbulent viscosity, μ_t/μ, were set to

0.1% and 0.1, respectively. Two sets of simulations are conducted using the k-ω and the q-s models. The first set of simulations utilizes the Venkatakrishnan limiter while the second set utilizes the MLP-u2 limiter. For each set, the effect of various settings of the K_{TM} limiter constant is examined. A CFL number of 100 is used.

The prediction accuracy is reflected in the comparison of the calculated surface pressure coefficient with the experimental results, as presented in Fig. 8. The results obtained from the two turbulence models are indistinguishable, and the agreement between the computational and experimental results is excellent. Note that the good agreement is also evident at the slat trailing edge. This agreement between the calculated pressure coefficient and the experiment on the slat trailing edge could not have been obtained with the commonly used sharp trailing edge (see for example [33]).
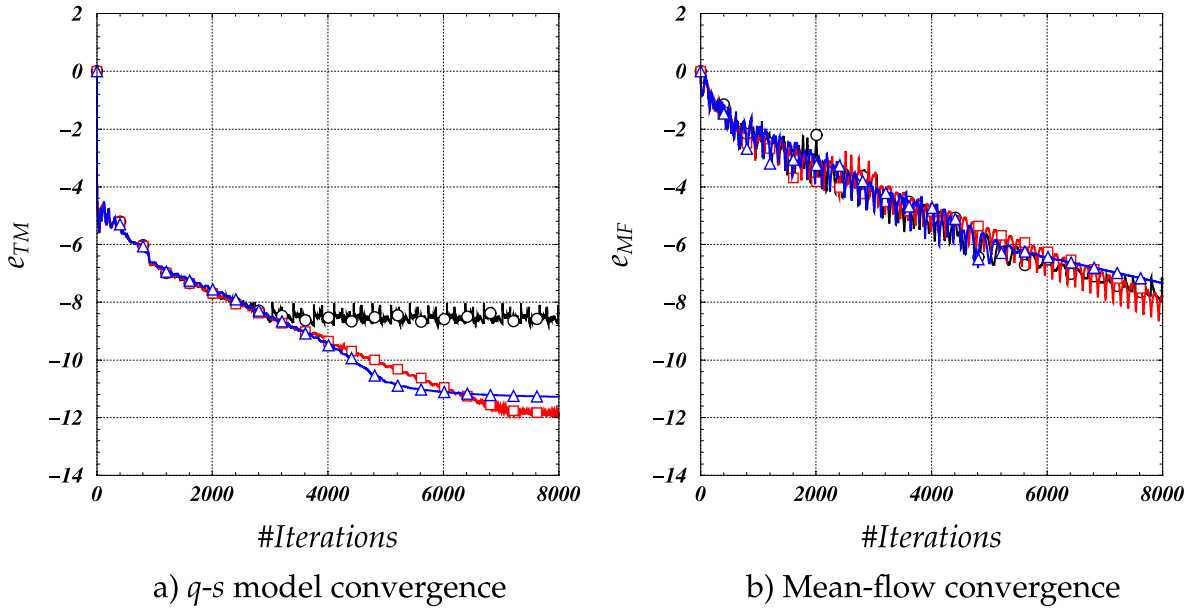
Fig. 20. Convergence histories from flow simulations about the NACA0012 airfoil with the unstructured grid using the q-s model and the Venkatakrishnan limiter; $K_{TM} = 0.5$: —△——△—, $K_{TM} = 2$: —□——□—, $K_{TM} = 5$: —○——○—.
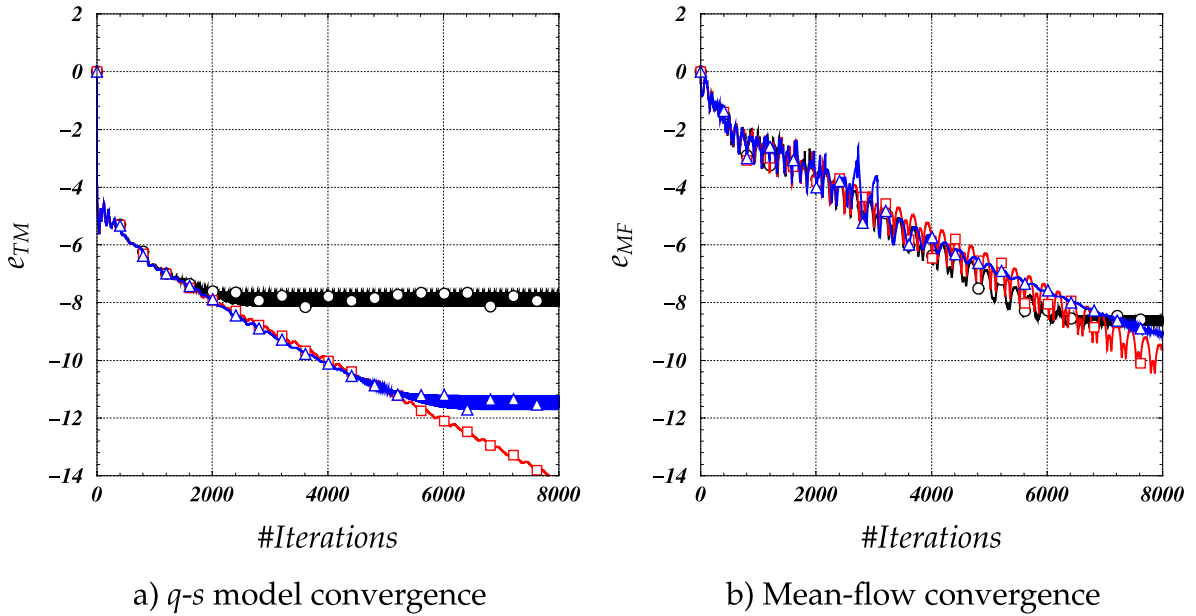

Fig. 21. Convergence histories from flow simulations about the NACA0012 airfoil with the unstructured grid using the q-s model and the *MLP-u2* limiter; $K_{TM} = 0.5$: —△——△—, $K_{TM} = 2$: —□——□—, $K_{TM} = 5$: —○——○—.

A comparison of convergence histories recorded in the simulations using the k-ω model with the Venkatakrishnan limiter is shown in Fig. 9. The convergence pattern of the turbulence model equations shows distinct oscillations with strong spikes, regardless of the values of limiter constant. Theoretically, reducing the value of the limiter constant may add numerical dissipation into the solution. However, this is not reflected in the turbulence model convergence pattern. The convergence of the mean-flow equations stalls at 4–5 orders of magnitude for all cases. Interestingly, the mean-flow residual obtained from the simulation using $K_{TM} = 2$, exhibits the poorest convergence level.

Fig. 10 shows the convergence behavior obtained from the simulations using the k-ω model with the *MLP-u2* limiter. Generally, the use of the *MLP-u2* limiter results in a significantly improved convergence

behavior. As expected, reducing the limiter constant, K_{TM}, improved the convergence level of the turbulence model equations. Moreover, the improved convergence of the turbulence model is also reflected in a significant improvement of the mean-flow equations. Overall, the convergence pattern shows a consistent dependency on the limiter constant.

Figs. 11 and 12 shows the convergence behavior obtained from the simulations using the q-s turbulence model with the Venkatakrishnan and *MLP-u2* limiters, respectively. A clear dramatic improvement in the convergence characteristics is shown. Foremost evident is that the q-s model exhibits a significantly reduced sensitivity to the limiter type or to the limiter constant values. With both limiters, and regardless of the values of K_{TM}, the residual of the mean-flow equations drops approximately eight orders of magnitude.
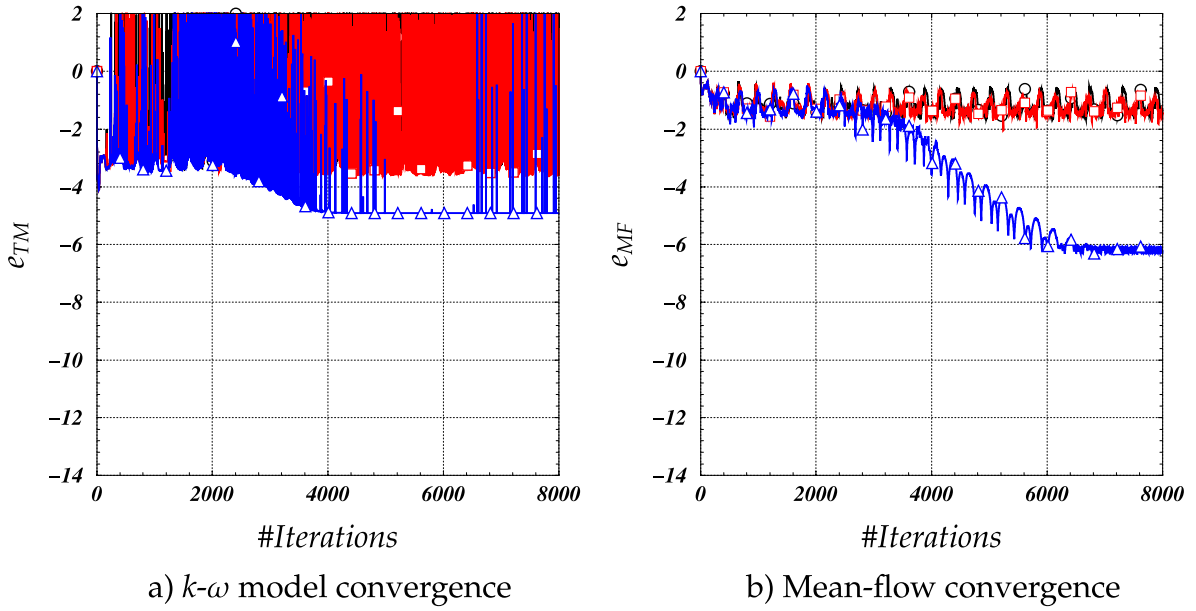
a) k-ω model convergence

b) Mean-flow convergence

Fig. 22. Convergence histories from flow simulations about the NACA0012 airfoil with the structured grid using the k-ω model and the Venkatakrishnan limiter; $K_{TM} = 0.5$: $\triangle$—$\triangle$, $K_{TM} = 2$: $\square$—$\square$, $K_{TM} = 5$: $\bigcirc$—$\bigcirc$.

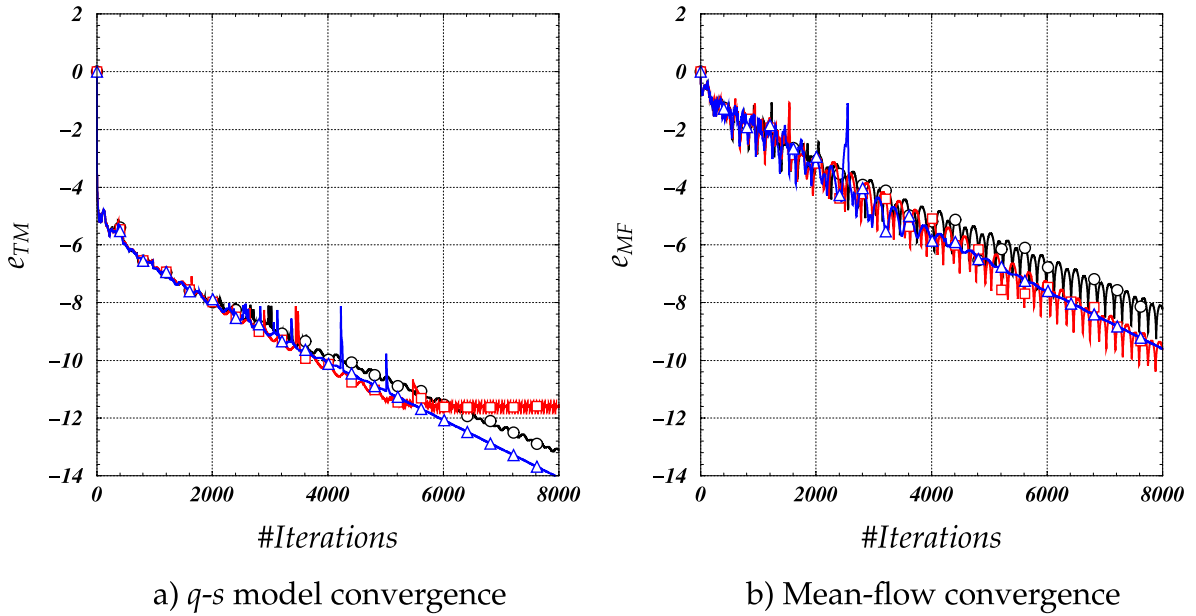a) q-s model convergence

b) Mean-flow convergence

Fig. 23. Convergence histories from flow simulations about the NACA0012 airfoil with the structured grid using the q-s model and the Venkatakrishnan limiter; $K_{TM} = 0.5$: $\triangle$—$\triangle$, $K_{TM} = 2$: $\square$—$\square$, $K_{TM} = 5$: $\bigcirc$—$\bigcirc$.

It should be noted that although the q-s model is obtained through an exact transformation of the k-ω model, the numerical equivalence of the solution is questionable [25]. One critical relevant issue is the influence of the limiter on the solution. Fig. 13 shows a map of the *MLP-u*2 limiter using $K_{TM} = 2$ that is applied to the reconstruction of k and q. Note that the limiter map is scaled between 0.2 to 1.0. Surprisingly, the limiter distribution of k displays irregular behavior, especially at the far field. Moreover, using the variable q results in a significantly reduced activation of the limiter.

Another measure that may highlight the impact of the limiter type on the turbulence model is the convergence of the aerodynamics forces, specifically, the convergence of the lift coefficient. Fig. 14 shows the lift coefficient histories obtained from the simulations using the k-ω turbulence model with the Venkatakrishnan and *MLP-u*2 limiters.

The results obtained using the Venkatakrishnan limiter (Fig. 14 (*a*)) exhibit a non-convergent behavior of the lift coefficient. For all three values of K_{TM}, the lift coefficient reaches an oscillatory behavior at about 3,500 iterations. Based on the residual convergence behavior (Fig. 9), the use of a limiter constant of $K_{TM} = 2$ results in the poorest lift coefficient convergence characteristics. An improvement in the convergence behavior of the lift coefficient is obtained when the *MLP-u*2 limiter is used. Except for certain minor oscillations that are present when using the highest value of K_{TM}, for all three values, a faster lift coefficient convergence is obtained.

In contrast, by using the q-s model, a far superior lift coefficient convergence characteristics are obtained, as shown in Fig. 15. For all limiter constants, and regardless of the limiter type, an oscillation free lift coefficient convergence is obtained.
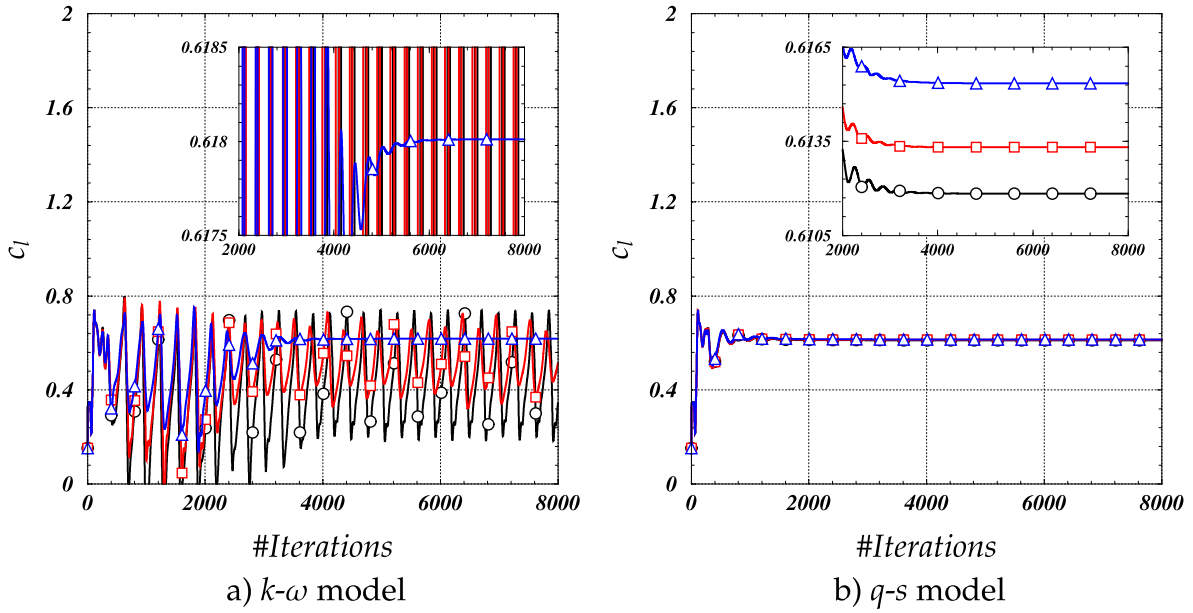
Fig. 24. Lift coefficient histories from flow simulations about the NACA0012 airfoil with the structured grid using the Venkatakrishnan limiter; K_{TM} = 0.5: —△——△—, K_{TM} = 2: —□——□—, K_{TM} = 5: —○——○—.

4.1.4. NACA0012 airfoil

Transonic flow involving shock induced separation is known to be numerically challenging. Two main difficulties can be indicated. First, accurately capturing the shock position and the subsequent extent of the separation. The second issue is the residual convergence difficulties which is the subject of the current work.

An experimental study about the symmetric NACA0012 airfoil at various transonic flow conditions was conducted by McDevitt and Okuno [34]. The experiment was carried out at the NASA Ames Research Center HRC facility. The NACA0012 airfoil chord length was c = 20.32 cm. The wind-tunnel tests were conducted for the evaluation of Reynolds number effects on the airfoil performance. The Reynolds number range of Re_∞ = 1–20 × 10^6 was addressed.

In the present work, the flow conditions correspond to a Reynolds number of Re_∞ = 10×10^6, an incidence angle of α = 3.91°, and the Mach number is set to M_∞ = 0.726. The free-stream turbulence intensity, Tu, and the normalized free-stream turbulent viscosity, μ_t/μ, were set to 0.1% and 0.1, respectively. A structured- and an unstructured-grids with a blunt trailing edge are used (shown in Fig. 16). The structured grid is an O-Type grid with the dimensions of 635×149 in the circumferential and normal directions, respectively. The first grid point neighboring the wall is placed at a distance of 2×10^{-6} of the airfoil chord (corresponds to a value of y_1^+ lower than 0.5). The unstructured grid that is used consists of 58,024 mixed-type elements. Near the wall, the unstructured grid is composed of the first 90 layers of the structured grid. Above these layers the grid consists of triangular and quadrilateral grid elements. The computational domain of the grids is extended to nearly 80 chord lengths from the airfoil surface. The simulations are conducted using a CFL number of 50. The Venkatakrishnan limiter and the *MLP-u*2 limiter are used with three values of the limiter constant, K_{TM} = 0.5, 2, and 5.

Fig. 17 contains a comparison between the calculated and the experimentally measured surface pressure coefficients [34]. The computed results are obtained from the simulations using the unstructured grid employing the *MLP-u*2 limiter with K_{TM} = 0.5. For all practical purposes, the computed surface pressure coefficient obtained from both models is the same. The computed results capture the location of the shock downstream of the experimentally measured shock location. A similar discrepancy was reported by Barakos and Drikakis using several turbulence models [35]. However, the pressure recovery after the shock is well predicted.

A comparison of convergence histories recorded in the simulations using the unstructured grid with the k-ω model and the Venkatakrishnan limiter is shown in Fig. 18. The residual of the governing equations shows the same characteristics as observed from the simulations about the NHLP-2D multi-element airfoil (Fig. 9 a)). Namely, the residual of the turbulence model exhibits strong spikes, and that of the mean-flow equations displays an oscillatory pattern. Moreover, using the highest value of K_{TM}, the mean-flow residual could not be reduced below one order of magnitude. Some improvement is achieved when using the *MLP-u*2 limiter, as shown in Fig. 19, and a reasonable convergence level is obtained only with the lowest limiter constant.

Figs. 20 and 21 show the residual convergence behavior that is obtained from the simulations using the unstructured grid with the q-s turbulence model while employing the Venkatakrishnan and *MLP-u*2 limiters, respectively. Similar to the observations made with the NHLP-2D case, a marked improvement in the convergence characteristics is obtained. Once again, the q-s model exhibits a significantly reduced sensitivity to the limiter type or to the limiter constant values. With both limiters, and regardless of the values of K_{TM}, the residual of the mean-flow equations drops about eight orders of magnitude.

The aim of the additional simulations using the structured grid is to examine whether the sensitivity to the limiter type is grid dependent. These simulations were conducted with the Venkatakrishnan limiter only. Figs. 22 and 23 show a comparison of convergence histories obtained from the simulations using the structured grid. Overall, the convergence characteristics that are obtained are similar to those obtained from the simulations using the unstructured grid. One exception is that when using the structured grid with the k-ω model, a reasonable convergence is obtained with the lowest limiter constant. Overall, the q-s model shows consistent and improved convergence characteristics.

Fig. 24 shows the lift coefficient histories obtained from the simulations using the structured grid. As expected, there is a correlation between the residual convergence and the lift convergence. While using the q-s model, a fully converged lift coefficient is obtained; while with the k-ω model the lift force is converged only with the lowest limiter value. As a means for comparison, consider the lowest value of K_{TM} = 0.5, a faster convergence is obtained using the q-s model. It should be emphasized that when using the k-ω model with high values of the limiter constant, the solution exhibits an oscillatory flow field instead of steady-state one. As a result, the lift coefficient exhibits an oscillatory behavior.

5. Conclusions

A square-root transformation that is applied to a k-ω model is proposed. The transformation stems from the encountered numerical difficulties that are common to second order accurate schemes for the turbulence model equations when using unstructured grids. The specific choice of the proposed model working variables aims to smooth the turbulence model dependent variables. Using the full transformation strategy, the transformed model accurately reproduce the baseline k-ω model performance. Moreover, the advantage of the alternative formulation is in its significant reduction of sensitivity to the limiter type. Due to this reduced sensitivity, the convergence characteristics of the transformed model are significantly improved. As a result, the aerodynamic forces converge twice as fast compared to the force convergence that is obtained using the baseline k-ω model. Overall, the transformed model is found to be significantly more reliable for computations on unstructured grids. Although the present work focuses on a specific k-ω model, the square-root transformation may be beneficial for other k-ω models.

References

[1] Jongen T, Marx YP. Design of an unconditionally stable, positive scheme for the k-ϵ and two-layer turbulence models. Comput & Fluids 1997;26(5):469–87.

[2] Park SH, Kwon JH. Implementation of k-ω turbulence models in an implicit multigrid method. AIAA J 2004;42(7):1348–57.

[3] Singh Sandhu JP, Girdhar A, Ramakrishnan R, Teja R, Ghosh S. A convergence study of solutions using two two-equation RANS turbulence models on a finite volume solver for structured grids. In: AIAA aviation, Atlanta, Georgia, AIAA paper 2018 - 3859, 2018.

[4] Chassaing JC, Gerolymos GA, Vallet I. Efficient and robust Reynolds-stress model computation of three-dimensional compressible flows. AIAA J 2003;41(5):763–73.

[5] Wang S, Dong Y, Deng X, Wang G, Wang J. High-order simulation of aeronautical separated flows with a Reynolds stress model. J Aircr 2018;55(3):1177–90.

[6] Basara B. Employment of the second-moment turbulence closure on arbitrary unstructured grids. Internat J Numer Methods Fluids 2004;44(3):377–407.

[7] Jalali A, Ollivier-Gooch C. Higher-order unstructured finite volume RANS solution of turbulent compressible flows. Comput & Fluids 2017;143:32–47.

[8] Mor-Yossef Y. Robust turbulent flow simulations using a Reynolds-stress-transport model on unstructured grids. Comput & Fluids 2016;129:111–33.

[9] Kok JC. Resolving the dependence on freestream values for the k-ω turbulence model. AIAA J 2000;38(7):1292–5.

[10] Coakley TJ, Huang PG. Turbulence modeling for high speed flows. In: 30th AIAA aerospace sciences meeting and exhibit, Reno, NV, AIAA paper 92 - 0436, 1992.

[11] Jiang L, Tabor G, Gao G. A new turbulence model for separated flows. Int J Comput Fluid Dyn 2011;25(8):427–38.

[12] Goldberg U, Batten P, Palaniswamy S. The q-l turbulence closure for wall-bounded and free shear flows. In: 42nd AIAA aerospace sciences meeting and exhibit, Reno, NV, AIAA paper 2004-0269, 2004.

[13] Durbin PA. On the k-ϵ stagnation point anomaly. Int J Heat Fluid Flow 1996;17(1):89–90.

[14] Durbin PA. Limiters and wall treatments in applied turbulence modeling. Fluid Dyn Res 2009;41(1):012203.

[15] Schumann U. Realizability of Reynolds-stress turbulence models. Phys Fluids 1977;20:721–5.

[16] Mokhtarpoor R, Heinz S. Dynamic large eddy simulation: Stability via realizability. Phys Fluids 2017;29(10):105104.

[17] Jawahar P, Kamath H. A high-resolution procedure for Euler and Navier-Stokes computations on unstructured grids. J Comput Phys 2000;164(1):165–203.

[18] Mor-Yossef Y. AUFSR+: Low mach number enhancement of the AUFSR scheme. Comput & Fluids 2016;136:301–11.

[19] Batten P, Leschziner MA, Goldberg UC. Average-state Jacobians and implicit methods for compressible viscous and turbulent flows. J Comput Phys 1997;137(1):38–78.

[20] Venkatakrishnan V. Convergence to steady state solutions of the Euler equations on unstructured grids with limiters. J Comput Phys 1995;118(1):120–30.

[21] Park JS, Kim C. Multi-dimensional limiting process for finite volume methods on unstructured grids. Comput & Fluids 2012;65:8–24.

[22] Mor-Yossef Y, Levy Y. The unconditionally positive-convergent implicit time integration scheme for two-equation turbulence models: Revisited. Comput & Fluids 2009;38(10):1984–94.

[23] Mor-Yossef Y. Unconditionally stable time marching scheme for Reynolds stress models. J Comput Phys 2014;276:635–64.

[24] Swanson RC, Turkel E, Rossow C-C. Convergence acceleration of Runge-Kutta schemes for solving the Navier–Stokes equations. J Comput Phys 2007;224(1):365–88.

[25] Langer S, Swanson RC. On boundary-value problems for RANS equations and two-equation turbulence models. J Sci Comput 2020;85(1):1–33.

[26] Mor-Yossef Y. A stable, positivity-preserving scheme for cross-diffusion source term in RANS turbulence models: Application to k-ω turbulence models. Comput & Fluids 2019;191:104234.

[27] Menter FR. Zonal two equation k-ω turbulence models for aerodynamic flows. In: 24rd AIAA fluid dynamics conference, Orlando, FL, AIAA paper 93 - 2906, 1993.

[28] Bachalo WD, Johnson DA. Transonic, turbulent boundary-layer separation generated on an axisymmetric flow model. AIAA J 1986;24(3):437–43.

[29] Turbulence Modeling Resource, http://turbmodels.larc.nasa.gov/index.html.

[30] Buice CU, Eaton JK. Experimental investigation of flow through an asymmetric plane diffuser. J Fluids Eng 2000;122:433–5.

[31] Gerolymos GA, Lo C, Vallet I, Younis BA. Term-by-term analysis of near-wall second-moment closures. AIAA J 2012;50(12):2848–64.

[32] Moir I. Measurements on a two-dimensional airfoil with high lift devices: A selection of experimental test cases for the validation of CFD codes. 1994, AGARD-AR-303.

[33] Balaji R, Bramkamp F, Hesse M, Ballmann J. Effect of flap and slat riggings on 2-D high-lift aerodynamics. J Aircr 2006;43(5):1259–71.

[34] McDevitt JB, Okuno AF. Static and dynamic pressure measurements on a NACA 0012 airfoil in the ames high Reynolds number facility. Vol. 2485, National Aeronautics and Space Administration, Scientific and Technical; 1985.

[35] Barakos G, Drikakis D. Numerical simulation of transonic buffet flows using various turbulence closures. Int J Heat Fluid Flow 2000;21(5):620–6.